lubricants

MDPI

Article

Flow Characteristics and Experimental Verification of T-Groove Dry Gas Seal Under Different Flow States

Lanxia Zhang [1], Xuexing Ding [1,*], Shipeng Wang [2] and Shuai Zhang [1]

[1] College of Petrochemical Engineering, Lanzhou University of Technology (LUT), Lanzhou 730050, China; zhanglanxia2021@163.com (L.Z.); zsbuct09@163.com (S.Z.)

[2] State Key Laboratory of Tribology in Advanced Equipment, Department of Mechanical Engineering, Tsinghua University, Beijing 100084, China; sp-wang@mail.tsinghua.edu.cn

* Correspondence: dingxxseal@126.com; Tel.: +86-150-0260-8287

Abstract: With the improvement of dry gas seal efficiency in high-parameter fields, the flow pattern of gas film lubrication is complicated. Based on gas lubrication theory, the Reynolds equation of compressible gas was established with a bidirectional T-groove dry gas seal as the research object. The Reynolds equation was solved to obtain a modified turbulent film pressure distribution law that affects gas lubrication. The effectiveness of the calculation program was verified by experimental tests. The results show that with an increase in operating parameters, the turbulence effect caused the gas film pressure fluctuation in the T-groove region to intensify, resulting in gas film flow instability. In addition, the inertia effect improved, which slowed down the leakage and affected the change law of stiffness and the rigid leakage ratio. When the fluid speed and gas pressure were low, the inertia effect could be ignored. When the groove depth was increased to 8 μm, the height difference between the trough and non-T-groove region became larger due to the combination of the turbulence and inertia effects. Further, when the gas film thickness was 3 μm, the opening force and gas film stiffness were high due to the dynamic pressure effect in the small film thickness groove. An increase in the gas film thickness weakened the turbulence effect and reduced the gas film pressure fluctuation.

Keywords: dry gas seal; turbulent flow; sealing performance; T-groove; inertial effect

check for updates

Received: 3 December 2024
Revised: 19 December 2024
Accepted: 28 December 2024
Published: 30 December 2024

Citation: Zhang, L.; Ding, X.; Wang, S.; Zhang, S. Flow Characteristics and Experimental Verification of T-Groove Dry Gas Seal Under Different Flow States. *Lubricants* **2025**, *13*, 9. https://doi.org/10.3390/lubricants13010009

1. Introduction

With the enhancement of dry gas seal efficiency in high-parameter fields, the lubrication state of seal clearance fluid flow gradually transitions from laminar to turbulent. The turbulent behavior considerably affects the gas flow, friction, and heat generation within gas seals, thereby influencing the stability and reliability of these seals. The inclusion of an inertia term in the Reynolds equation is crucial for accurately describing laminar and turbulent flows. Neglecting this term may lead to erroneous assessments of air flow patterns, resulting in calculation results that deviate from those observed under actual conditions [1–5]. Furthermore, disregarding the dependence of the inertia term on specific application flow conditions introduces considerable errors when using a solution model based on laminar flow assumptions and forced pressure boundary conditions to calculate dry gas seal lubrication film pressure [6]. To modify calculation models, Koga et al. [7] analyzed hydrostatic pressure seals under different conditions and obtained the trend of the pressure distribution on the sealing surface with respect to the inertia effect. Zhang et al. [8] proposed a Reynolds equation applicable to complex flow fields for a plane Couette flow field and introduced an inertia term directly into the closed analytical lubrication equation using a modified average method, obtaining a modified calculation model through experimental verification. In recent years, notable turbulence effects have been observed in microscale flow fields owing to changes in the Reynolds number of seal end faces under harsh working conditions. Shahin et al. [9] used a turbulence model and large eddy simulation to study laminar and turbulent flows for identifying factors influencing gas film flow characteristics and performance. To accurately predict dry gas seal characteristics, Hahn [10] and Park et al. [11] proposed a modified Reynolds equation considering laminar and turbulent flow effects and solved this equation using the finite element and Newton–Raphson methods to obtain optimal structural parameters. The aforementioned studies mainly focused on one-way sealing structures while analyzing the influence of inertial force or turbulent effects on microscale flow fields. Currently, with advanced sealing technology being widely applied, growing interest is being committed to studying interactions between influencing factors. Yan et al. [12,13] established a turbulent Reynolds equation under centrifugal inertia force. They reported that the opening force and leakage rate under turbulent flow were lower than those under laminar flow and the steady-state performance parameters changed with the working condition parameters under different flow modes, providing a reference for optimizing dry gas seal design. Wang et al. [14] derived a perturbation Reynolds equation using a perturbation method, analyzed the effects of turbulence and inertia on sealing performance, and found that turbulence considerably influenced the flow characteristics of low-viscosity fluids under high-speed conditions. Xu et al. [15] used the finite difference method to analyze the effect of inertia effect on the steady-state performance of different spiral-groove dry gas seals under laminar flow. They reported enhanced inertia effects under critical temperatures. The aforementioned studies indicate that the impact of different flow states on the distribution of multiflow fields, sealing efficiency, and stability of dry gas seal films under high-speed and high-pressure conditions cannot be disregarded.

During the start and stop stages of dry gas sealing devices, the inertia effect may result in uneven contact pressure in seal pair clearance, thereby affecting the effectiveness of these devices. Currently, research on bidirectional groove dry gas seals primarily focuses on steady-state performance analysis [16,17], dynamic characteristics [18], groove texture design [19–21], and optimization design for gas effects [22,23], among others. Simplified models based on laminar flow hypotheses are no longer applicable owing to the complex hydrodynamic behavior exhibited by dynamic pressure grooves. Considering the antireverse characteristics of bidirectional grooves can help mitigate friction issues with sealing width and end faces during the start and stop stages while improving the reliability of the rotating machinery. To adapt to various working conditions, it is necessary to study the flow characteristics of T-groove dry gas seals under modified turbulence effects. In this study, we established a compressible gas energy equation based on the gas lubrication theory for T-groove dry gas seal structures. The Reynolds equation that considers the interaction between centrifugal inertia force and turbulence effects was solved to obtain the film pressure distribution for the modified gas lubrication. Through numerical calculations and experimental tests, we compared and analyzed how working conditions and structural parameters influence gas film lubrication performance in dry gas seals while optimizing the structural parameters to meet the changing operating condition requirements; this provides theoretical references for accurate turbulence calculation models.

2. T-Groove Dry Gas Seal

2.1. Geometric Model

The structure of a double-end T-groove dry gas seal is shown in Figure 1. The sealing band comprises dynamic and static rings, which are installed on both sides of the rotating shaft. Typically, the sealing surface is made of a hard material to ensure excellent wear resistance and sealing effectiveness. The end face of the moving ring features a micron-level T-shaped shallow groove that facilitates gas pumping into the microgroove when the sealing ends rotate relative to each other. This effectively prevents gas flow in the circular direction through the sealing weir between the grooves, pressurizing the gas gap of the sealing pair to form a gas film with a certain stiffness. Consequently, the media leakage at the sealing end [24,25] decreases, which enhances the reliability and stability of the dry gas seal.

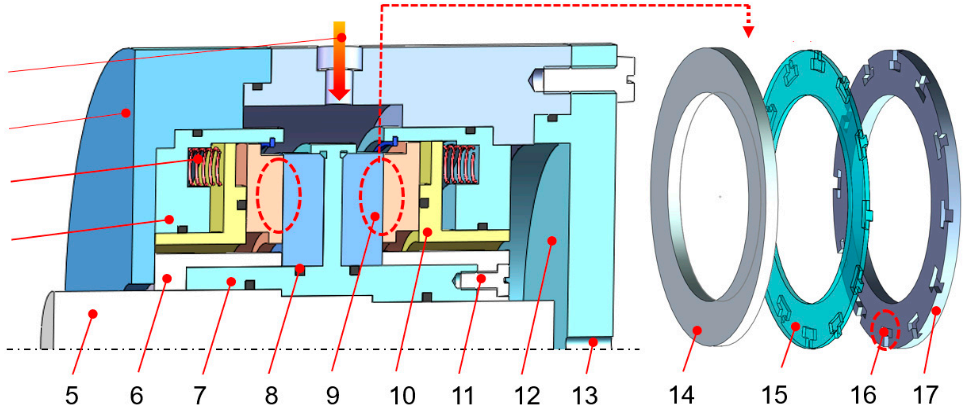

Figure 1. Schematic diagram of dry gas seal structure. 1—Buffer gas; 2—Sealing house; 3—Spring; 4—Spring seat; 5—Rotating shaft; 6—Pressing sleeve; 7—Shaft sleeve; 8—O-ring; 9—Stationary ring; 10—Thrust collar; 11—Fixing bolt; 12—End cover; 13—Flowmeter interface; 14—Stationary ring; 15—Gas film; 16—T-groove; 17—Rotating ring.

The T-groove end-face structure is shown in Figure 2. Owing to the symmetrical and periodic distribution of the T-grooves on the sealing width, only $1/N_g$ of the seal's end face is considered for the entire calculation area. Table 1 presents the initial calculation parameters, including r_t as the radius of the joint surface between the dynamic pressure and intake grooves, w_1 as the circumferential arc length of the intake groove, w_2 as the circumferential arc length of the dynamic pressure groove, w_3 as the arc length of the unslotted part between adjacent dynamic pressure grooves, and θ as development angle of the T-groove. The calculated structural parameters defining one-dimensional T-groove include α_1 as circumferential ratio, α_2 as groove width ratio, β_1 as radial ratio, and β_2 as groove length ratio. The expression relationship can be summarized accordingly.

$$\alpha_1 = \frac{w_1}{w_2},\ \alpha_2 = \frac{w_2}{w_2 + w_3},\ \beta_1 = \frac{r_o - rt}{r_o - r_g},\ \beta_2 = \frac{r_o - r_g}{r_o - r_i} \tag{1}$$

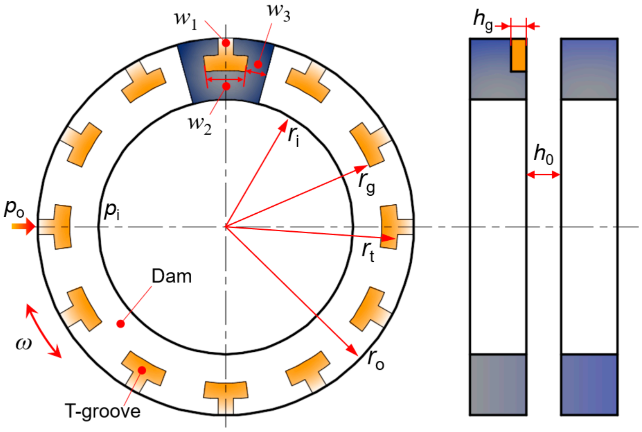

Figure 2. T-groove end-face structure.

Table 1. Initial calculation parameters of T-groove dry gas seal.

Parameters	Value	Parameters	Value
The inner radius of the rotating ring r_i/mm	58.42	T-groove length ratio β_2	0.88
The outer radius of the rotating ring r_o/mm	77.78	Number of T-grooves N_g	12
T-groove root radius r_g/mm	69	Inlet pressure p_i/MPa	2
Middle radius of T-groove r_t/mm	73.39	Outlet pressure p_o/MPa	0.1
T-groove width ratio α_2	0.5	Rotational speed n/rpm	20,000
Average gas film thickness h/μm	3.05	Fluid density $\rho_\mathrm{o}/\mathrm{kg{\cdot}m^{-3}}$	1.293
T-groove depth h_g/μm	5	Gas viscosity $\eta_\mathrm{o} \times 10^{-5}$/pa·s	1.81

2.2. Mathematical Model

2.2.1. Governing Equation

(1) Basic assumptions [26–28]:

- (a) The effects of volumetric forces, such as gravity, are negligible.
- (b) The effects of slip flow and roughness on the trough bottom are negligible.
- (c) The heat exchange caused by interfacial heat conduction is ignored.
- (d) The thermal deformation due to the heat generated by the sealing ring is negligible.

(2) In turbulent flow state, the compressible Reynolds equation considering the centrifugal inertia force effect is given by Formula (2). In a flow field with a low Reynolds number, the turbulence coefficient is described by an improved transition function. When the local Reynolds number R_h is $\geq$1360, the flow is completely turbulent [29].

$$\frac{1}{r}\frac{\partial}{\partial\theta}\left(G_\theta\frac{\rho h^3}{\eta}\frac{\partial p}{\partial\theta}\right)+\frac{\partial}{\partial r}\left(G_\mathrm{r}\frac{r\rho h^3}{\eta}\frac{\partial p}{\partial r}\right)=6\omega r\frac{\partial}{\partial\theta}(\rho h)+\frac{\partial}{\partial r}\left[G_\mathrm{r}\frac{\rho^2r^2\omega^2h^3}{\eta}(\frac{1}{4}+\lambda)\right]+12r\frac{\partial}{\partial t}(\rho h) \tag{2}$$

where p—pressure, MPa; h—average gas film thickness, μm; η—viscosity, Pa·s; ρ—gas density, kg/m^3; ω—moving ring angular velocity rad/s; λ—inertia coefficient; R_h—local Reynolds number; G_θ—circumferential turbulence coefficient; G_r—radial turbulence coefficient.

In this paper, the Ng-Pan turbulence model was used. When the flow with $R_\mathrm{h} < 900$ is regarded as laminar flow, the circumferential turbulence coefficient and radial turbulence coefficient are equal, that is, $G_\theta = G_\mathrm{r} = 1/12$. When $R_\mathrm{h} \geq 1360$, the flow is fully turbulent, and the turbulence coefficient is expressed as

$$G_\theta=\frac{1}{12+0.0136{R_\mathrm{h}}^{0.9}};\ G_\mathrm{r}=\frac{1}{12+0.0043{R_\mathrm{h}}^{0.96}} \tag{3}$$

$$R_\mathrm{h}=\frac{\rho\omega rh}{\eta} \tag{4}$$

The centrifugal inertia effect in the dry gas seal cannot be ignored. According to the relevant theory of Constantinescu [30], an inertial correction coefficient λ is introduced to realize the conversion of laminar flow and turbulent flow state. The specific expression of the transition function of the inertia coefficient is as follows:

$$\lambda=0.0764-0.0142\mathrm{Tanh}\left[\frac{4(R_\mathrm{h}-1130)}{1360-900}\right] \tag{5}$$

Considering the transition region from laminar flow to turbulent flow, when $R_\mathrm{h} < 900$, the local flow field is laminar flow, where $\lambda = 0.09$. When $R_\mathrm{h} \geq 1360$, the flow is turbulent, $\lambda = 0.885/R_h^{0.367}$.

2.2.2. Boundary Conditions

(1) Pressure boundary condition

$$\begin{cases} p(r_\mathrm{i},\theta) = p_\mathrm{i} \\ p(r_\mathrm{o},\theta) = p_\mathrm{o} \end{cases} \tag{6}$$

where p_i, p_o—pressure at inside and outside diameters; r_i, r_o—inner and outer radius of seal face.

(2) Periodic pressure conditions along the circumference

$$p(r,\theta) = p(r,\frac{2\pi}{N_\mathrm{g}} + \theta) \tag{7}$$

2.3. Steady-State Performance Parameters

Opening force of sealing pair's end face:

$$F_\mathrm{o} = \int_0^{2\pi}\int_{r_\mathrm{i}}^{r_\mathrm{o}} prdrd\theta \tag{8}$$

Gas mass leakage of the sealing pair's end face:

$$Q = \int_0^{2\pi} m\rho\left[-\frac{h^3}{12\eta}\frac{\partial p}{\partial r}\right]rd\theta \tag{9}$$

Gas film stiffness:

$$K = \frac{\partial F_\mathrm{o}}{\partial h} \tag{10}$$

Stiffness leakage ratio:

$$\mathit{\Gamma} = \frac{K}{Q} \tag{11}$$

2.4. Solving Governing Equation

2.4.1. Numerical Calculation Method

The Reynolds equation, being a nonlinear differential equation, poses challenges in obtaining an analytical solution. However, the use of numerical calculation methods offers flexibility and simplicity in implementation on computer systems. Figure 3 shows the grid division diagram of the central difference scheme, where p (i,j) denotes the gas film pressure at any point on the circular sealing pair's end face. To accommodate this circular geometry, a polar coordinate form is adopted with m grids for the circumferential division and n grids for the radial division.

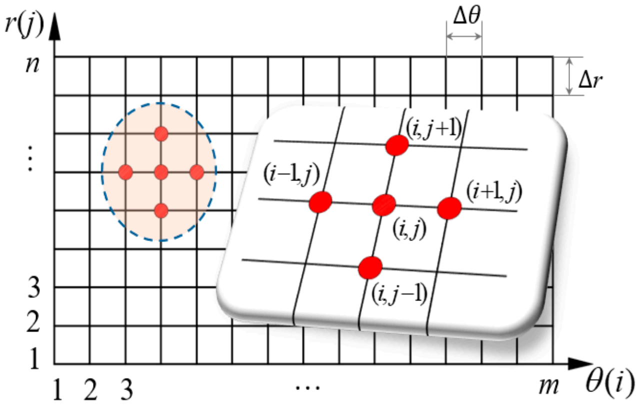

Figure 3. Grid division diagram of central difference scheme.

2.4.2. Dimensionless Definition

In order to make the calculation results of the equation more general, dimensionless parameters are constructed.

$$R = \frac{r}{r_o},\ P = \frac{p}{p_o},\ H = \frac{h}{h_0} \tag{12}$$

where R—dimensionless radius, P—dimensionless gas film pressure, H—dimensionless gas film thickness, and h_0—the thickness of the gas film in the non-T-groove region.

2.4.3. Discretization of Governing Equations

The central difference scheme and upwind scheme of the five-point difference method are used to discretize the dimensionless turbulent Reynolds equation. The discrete format of P at coordinates P (i, j) is as follows:

$$\begin{cases} \frac{\partial P}{\partial \theta} = \frac{P_{i+1,j}-P_{i-1,j}}{2\Delta\theta} \\ \frac{\partial P}{\partial R} = \frac{P_{i,j+1}-P_{i,j-1}}{2\Delta R} \end{cases} \qquad \begin{cases} \frac{\partial^2 P}{\partial \theta^2} = \frac{P^2_{i+1,j}-2P^2_{i,j}+P^2_{i-1,j}}{(\Delta\theta)^2} \\ \frac{\partial^2 P}{\partial R^2} = \frac{P^2_{i,j+1}-2P^2_{i,j}+P^2_{i,j-1}}{(\Delta R)^2} \end{cases} \tag{13}$$

To ensure the stability of the numerical solution and improve the accuracy of the calculation results when solving the difference equation of dry gas seal pressure control, the cubic mean representation of gas film thickness is considered with the following changes:

$$\begin{cases} H^3_{i+\frac{1}{2},j} = \frac{2H_{i+1,j}H_{i,j}}{H^3_{i+1,j}+H^3_{i,j}} \\ H^3_{i-\frac{1}{2},j} = \frac{2H_{i,j}H_{i-1,j}}{H^3_{i,j}+H^3_{i-1,j}} \end{cases} \qquad \begin{cases} H^3_{i,j+\frac{1}{2}} = \frac{2H_{i,j+1}H_{i,j}}{H^3_{i,j+1}+H^3_{i,j}} \\ H^3_{i,j-\frac{1}{2}} = \frac{2H_{i,j}H_{,ji-1}}{H^3_{i,j}+H^3_{i,j-1}} \end{cases} \tag{14}$$

A successive overrelaxation iteration scheme is used to solve this problem. During iteration, a small positive number ε is specified as the precision standard of the iterative convergence. This parameter is used to determine when the iteration reaches the end condition: when the relative error between the results of two successive iterations falls to ε or below, the solution is considered sufficiently close to the true value to terminate the iteration process. Here, ε is regarded as the threshold of convergence accuracy.

$$\frac{\sum\limits_{n}^{j=1}\sum\limits_{m}^{i=1}\left|P_{i,j}^{(k+1)} - P_{i,j}^{(k)}\right|}{\sum\limits_{n}^{j=1}\sum\limits_{m}^{i=1}\left|P_{i,j}^{(k)}\right|} \le \varepsilon; \qquad \frac{\sum\limits_{n}^{j=1}\sum\limits_{m}^{i=1}\left|H_{i,j}^{(k+1)} - H_{i,j}^{(k)}\right|}{\sum\limits_{n}^{j=1}\sum\limits_{m}^{i=1}\left|H_{i,j}^{(k)}\right|} \le \varepsilon \tag{15}$$

3. Numerical Calculation Process

The density and viscosity of gas under different parameters were obtained from calculations using the software REFPROP V 9.0. After dividing the grid, the initial flow field and boundary conditions were set. Considering the inertia and turbulence effects, based on the gas lubrication theory, the finite difference method was used to solve the governing equation, and the flow field characteristics under different flow modes were obtained. The calculation process of the T-groove dry gas seal is shown in Figure 4.

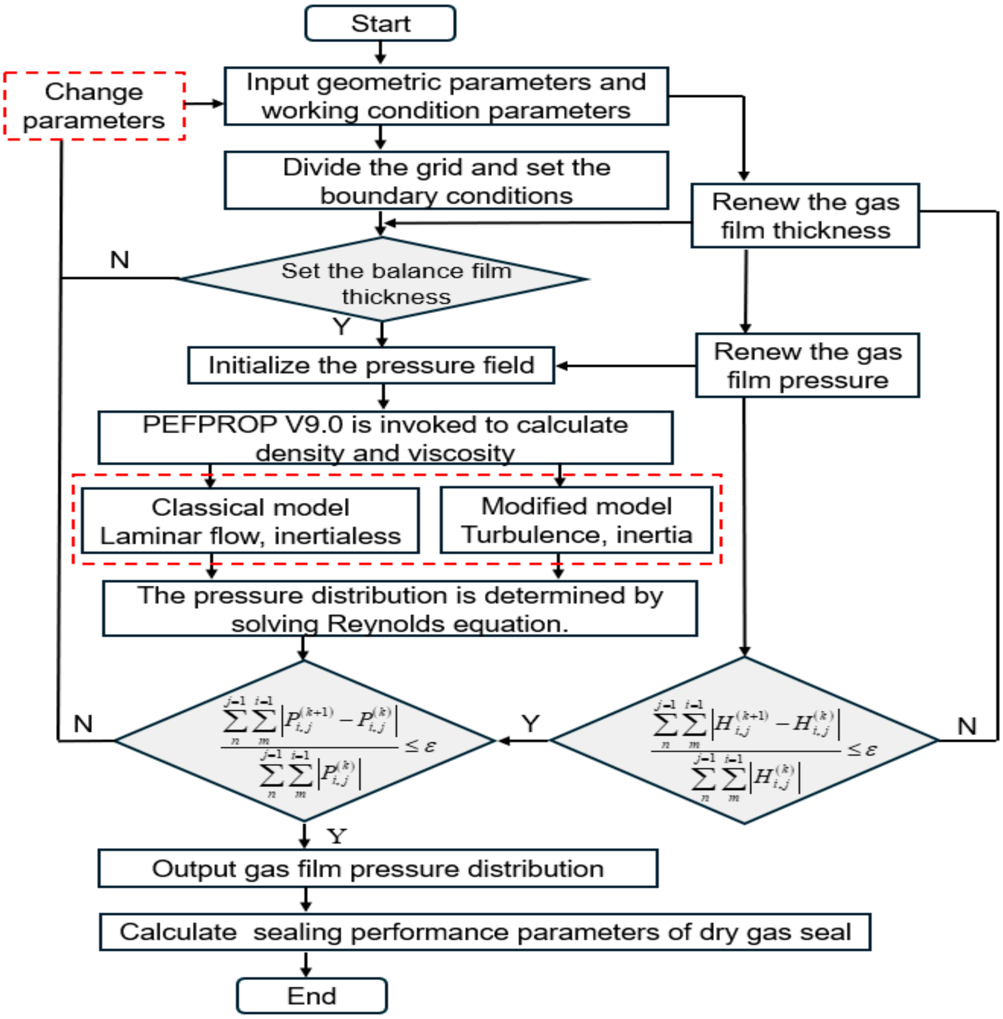

Figure 4. The calculation process of T-groove dry gas seal.

4. Experimental Research

4.1. Dry Gas Seal Experimental Device

Figure 5 shows the dry gas seal experimental device comprising a testing system, an auxiliary testing system, and a control measurement system. The testing method involves intermediate air intake, double-end installation, and single-end testing. A high-pressure buffer gas is supplied via the compressor while the test medium gas enters the compressor through the filter and subsequently reaches the sealed chamber via the gas path system. The pressure-reducing valve at the entrance regulates the gas pressure within. An auxiliary dry gas seal for testing is positioned near the motor side to prevent any gas leakage into the atmosphere after the gas flows into the chamber. Speed control is achieved using a frequency converter housed in a control cabinet. Instruments or sensors are used to monitor the data acquisition of signals related to medium pressure, speed, and leakage rate, which are analyzed and processed by a computer based on these data signals.

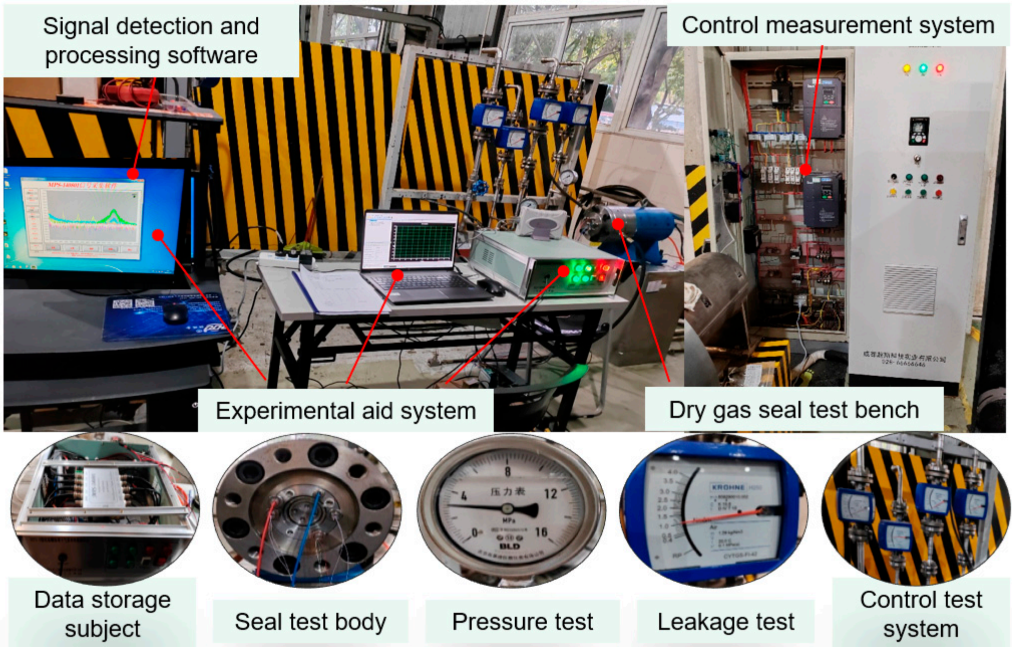

Figure 5. Dry gas seal experimental device system.

4.2. Dry Gas Seal Test Technology

The T-groove dry gas seal test piece is depicted in Figure 6. Tungsten carbide serves as the material for the moving ring, while the static ring is equipped with a test sensor at its rear end. The material used is graphite. The test system is assembled and configured according to the design requirements, adjusting the medium in the sealing chamber via a pressure-reducing valve. Upon gas stabilization, manual turning is performed before installing the end cover of the sealing chamber to initiate testing. The key performance parameters for this test primarily include the clearance leakage rate and opening force of the sealing pair. In particular, leakage rate testing is crucial for evaluating dry gas seal performance. To ensure measurement accuracy, a KROHNE H250 metal tube float flowmeter with an accuracy class and a measuring range of 1.5 and 16 Nm^3/h, respectively, was selected. In addition, an eddy current displacement sensor was used to measure axial displacement and changes thereof to evaluate the opening force of the sealing device; this sensor also enables real-time monitoring of dry gas seal operation so that timely adjustments can be made to optimize the working conditions and achieve optimal sealing effectiveness.

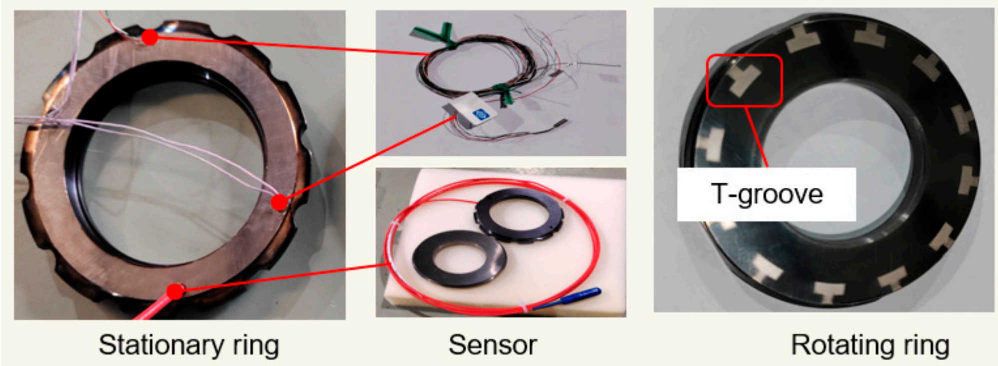

Figure 6. T-groove dry gas seal test piece.

5. Results and Analysis

5.1. Grid Independence and Model Validity Verification

The grid independence verification is shown in Figure 7. As the number of grids gradually increased, the opening force and leakage rate increased. However, when the number of grids reached 155 × 155, the performance curve under the turbulence model began plateauing, indicating a stable variation pattern of the performance parameters. Considering the complexity of the calculation model and ensuring efficient computation within an acceptable accuracy range, a grid size of 195 × 195 was selected.

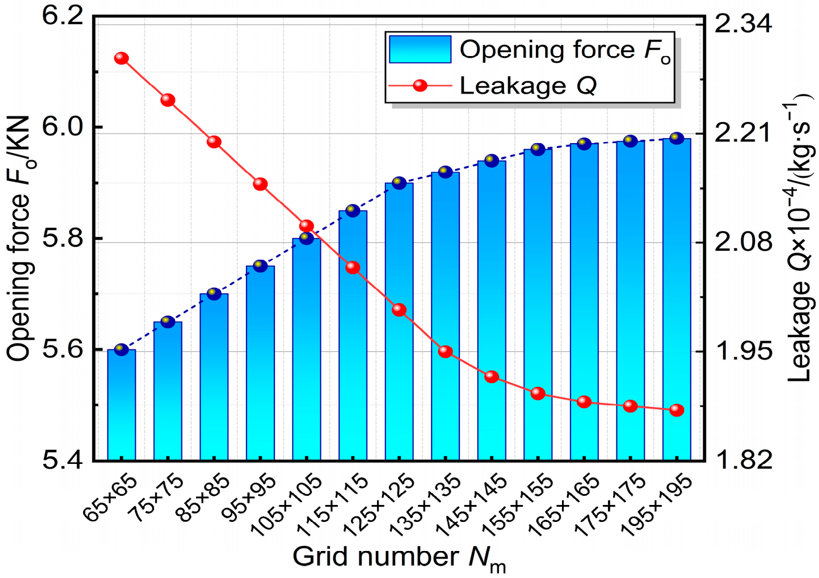

Figure 7. Grid independence verification.

The variation of leakage with medium pressure with respect to the inertia effect, noninertia effect, literature parameters [31], and experimental test is shown in Figure 8a. As the seal pressure differential force increased from the outer diameter to the inner diameter, gas leakage increased with increasing pressure. This figure shows that the leakage rate with the inertia effect was lower than that without the inertia effect, attributable to the centrifugal inertia force acting from the inner diameter to the outer diameter, which opposed the flow direction and "hindered" gas flow. With the inertia effect, the maximum relative errors between the leakage and literature parameter and experimental values were 4.68% and 3.85%, respectively. These results validate the accuracy of the proposed model within a range of calculation precision.

The variations of the laminar flow and turbulent flow mode, literature parameter [32], and experimental leakage with increasing medium pressure are shown in Figure 8b. The joint action of the gas flow in a turbulent flow resulted in a more uniform pressure distribution within the seal gap and reduced the pressure difference, thereby decreasing the leakage rate. In the laminar flow state, the gas flow was more stable but increased the local pressure differences, which easily increased the leakage rate. Under the classical laminar flow model, maximum relative errors of 18.9% and 14.71% were observed between the leakage and literature parameter and experimental values, respectively, exceeding the acceptable accuracy limits. However, under the turbulence-modified model, these maximum relative errors decreased to 0.96% and 5.38%, respectively, falling within an acceptable accuracy range. Therefore, we used the turbulence-modified model to analyze the flow characteristics of T-groove dry gas seals.

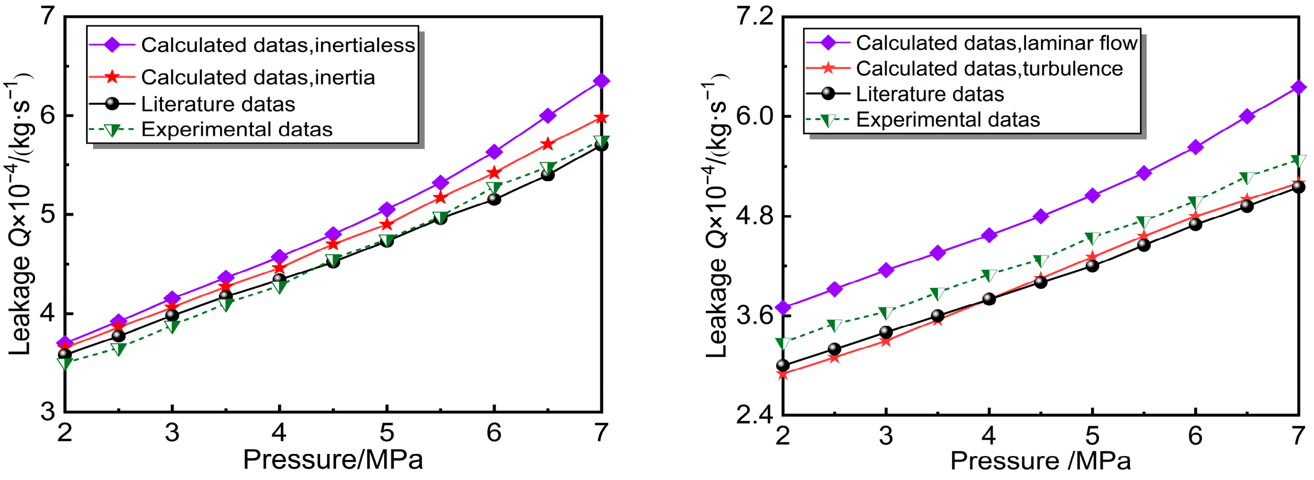

(**a**) Inertial effect (**b**) Turbulence effect

Figure 8. Validity verification of the calculation program considering inertia and turbulence effects.

5.2. Distribution of Membrane Pressure

Figure 9 shows the film pressure distribution law of the T-groove dry gas seal with respect to pressure; the initial calculation parameters are shown in Table 1. As shown in the figure, under the same pressure p_o, the film pressure distribution affected by turbulent flow in the T-groove was larger than that affected by laminar flow. However, the film pressure distribution in the non-T-groove region was relatively stable. When p_o = 1 MPa, the local low-pressure area near the T-groove was significant. With an increase in medium pressure, the turbulent effect intensified the gas film's response to a change in the film pressure. When p_o = 4 MPa, the gas film thickness was relatively reduced, which affected the gas film pressure distribution. The turbulence effect caused the gas film pressure to pulsate. The gas velocity and pressure fluctuated, resulting in the pressure in the local area of the gas film (local gas film pressure) being lower than the average pressure. This pulsation may affect the stability and sealing performance of the gas film. In addition, the turbulence effect increased the moisture transfer of the fluid, which increased the nonuniformity of the gas film pressure. Further, local high pressure easily occurred in the rapidly changing part of the T-groove structure, and the change in the air flow pattern in these high-pressure areas affected the film pressure distribution.

Figure 10 shows the film pressure distribution of the T-groove dry gas seal under different film thicknesses (h_0). The initial calculation parameters are shown in Table 1. When h_0 = 3 μm, a thin film caused the gas to generate a high flow rate, thereby increasing the local pressure. The membrane pressure gradient under the laminar flow was more conspicuous than that under the turbulent effect. In addition, the thin gas film and turbulent effect became unstable when the external disturbance changed, resulting in fluctuations in the inner membrane pressure of the T-groove. When h_0 = 5 μm, the gas flow resistance increased, resulting in a decrease in the gas flow speed inside the film, thereby reducing the local gas film pressure. In this case, the gas film pressure in the T-groove region under laminar flow was greater than that under turbulent flow. When h_0 = 9 μm, the gas flow tended to be laminar and the turbulent effect weakened, thereby reducing the pressure drop and fluctuation. This reduced fluctuation helped create a more uniform pressure distribution within the membrane, thereby reducing the formation of local high- and low-pressure areas and hence improving the T-groove flow stability. Therefore, the turbulence effect was weak when the gas film pressure was large. Furthermore, owing to the strong dynamic pressure effect in low film thickness grooves, the corresponding turbulent effects caused considerable changes in film pressure.

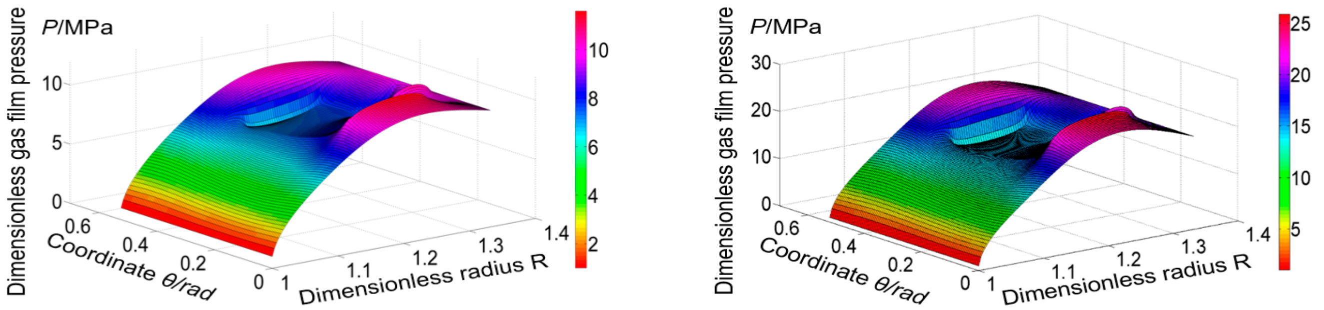

(**a**) Laminar flow $p_o = 1$ MPa (**e**) Turbulence $p_o = 1$ MPa

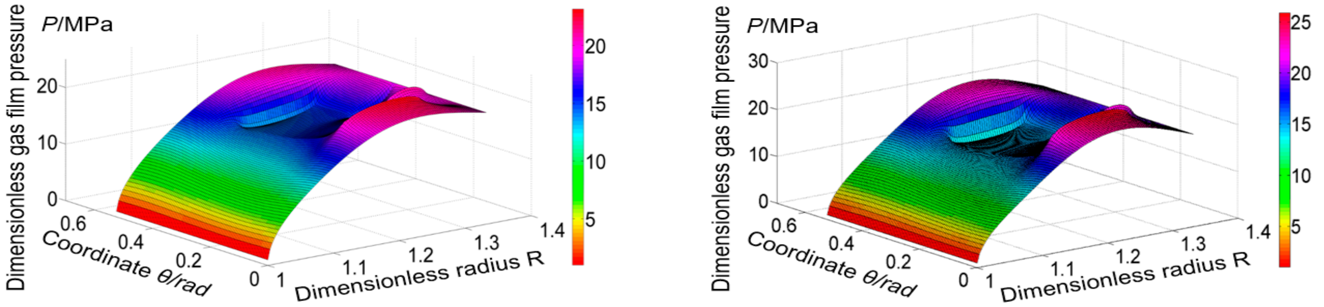

(**b**) Laminar flow $p_o = 2$ MPa (**f**) Turbulence $p_o = 2$ MPa

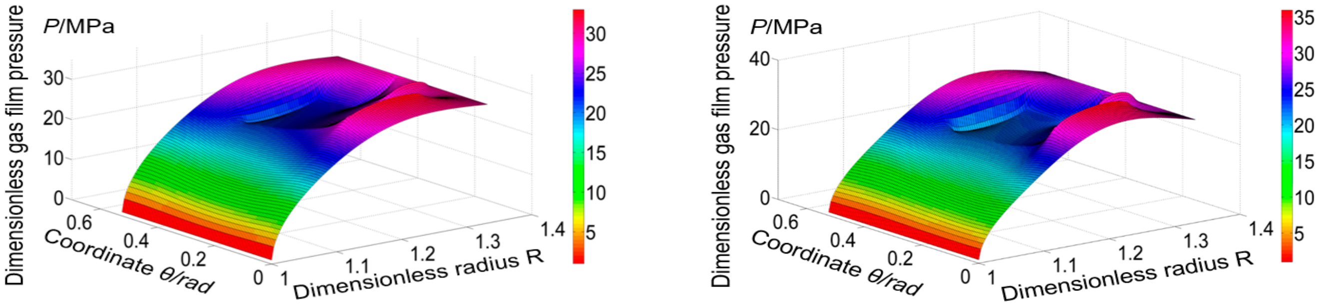

(**c**) Laminar flow $p_o = 3$ MPa (**g**) Turbulence $p_o = 3$ MPa

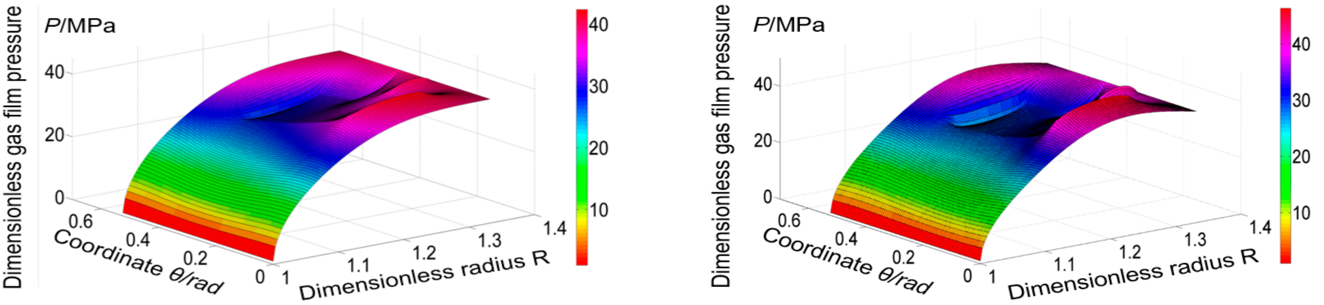

(**d**) Laminar flow $p_o = 4$ MPa (**h**) Turbulence $p_o = 4$ MPa

Figure 9. Influence of medium pressure variation on film pressure distribution.

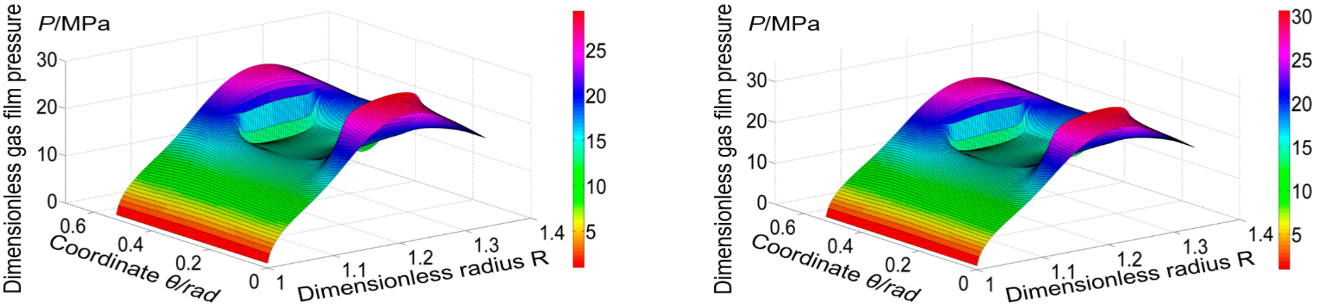

(**a**) Laminar flow h_0 = 3 μm (**e**) Turbulence h_0 = 3 μm

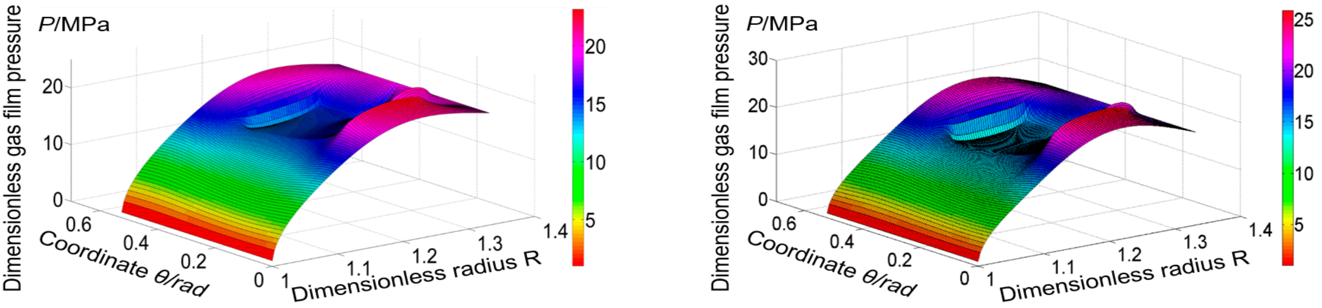

(**b**) Laminar flow h_0 = 5 μm (**f**) Turbulence h_0 = 5 μm

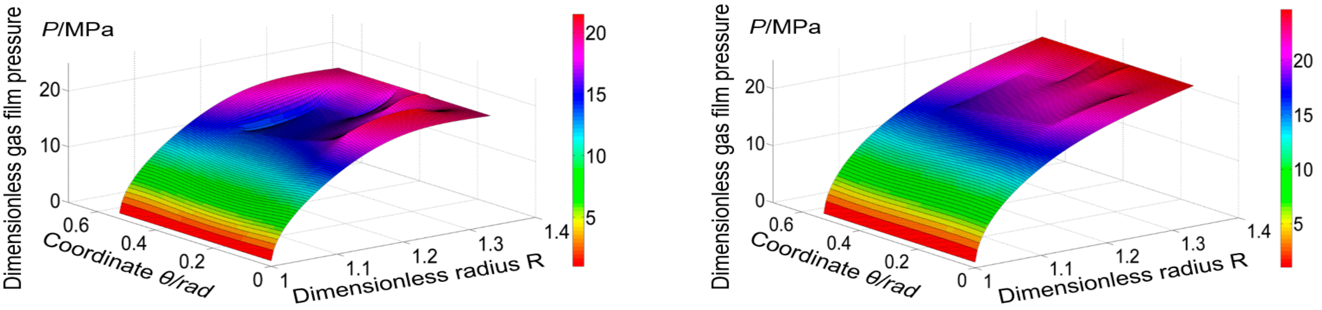

(**c**) Laminar flow h_0 = 7 μm (**g**) Turbulence h_0 = 7 μm

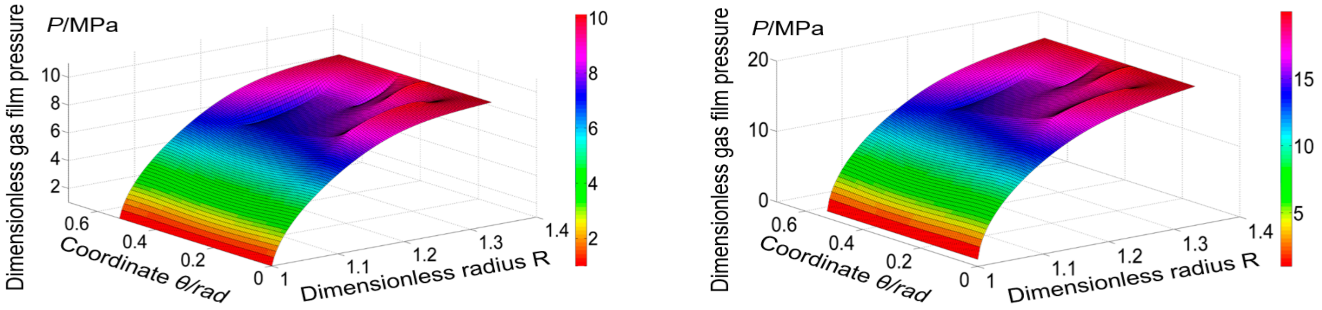

(**d**) Laminar flow h_0 = 9 μm (**h**) Turbulence h_0 = 9 *μm*

Figure 10. Effect of gas film thickness variation on film pressure distribution.

5.3. Analysis of Influencing Factors

5.3.1. Effect of Rotational Speed on Sealing Performance

Figure 11 shows the variation of dry gas seal performance parameters with respect to speed. Figure 11a shows that the opening force under different flow modes increased with increasing rotational speed (n). When n = 10,000 rpm, the opening forces under the laminar and turbulent flow modes were 6.30 and 6.35 KN, respectively. At n = 40,000 rpm, the opening forces under the laminar and turbulent flow modes increased by 0.7% and 3.1%, respectively. The main reason the opening force under the laminar flow mode decreased with varying rotational speed is that the turbulent effect considerably increased at high speed, leading to the gas film pressure fluctuation, thereby affecting the opening force. Figure 11b shows that the leakage increased first and then gradually decreased with increasing speed. When the speed was low, the influence of inertia was small. With an increase in speed, the inertia effect was enhanced, and the degree of "obstruction" was strengthened so that the leakage was weakened. Considering the turbulent effect, the radial mean velocity decreased, resulting in a lower leakage in turbulent flow than in laminar flow. Figure 11c shows that the gas film stiffness increased with increasing rotational speed, and the turbulence and inertia effects increased the pressure gas film fluctuation, resulting in the gas film stiffness instability. Figure 11d shows that the rigid leakage ratio gradually decreased with increasing n. An increase in the turbulence effect led to an uneven gas film thickness and increased the leakage amount. Furthermore, the enhanced inertia effect increased the complexity if the dynamic behavior of the gas film and further decreased the rigid leakage ratio.

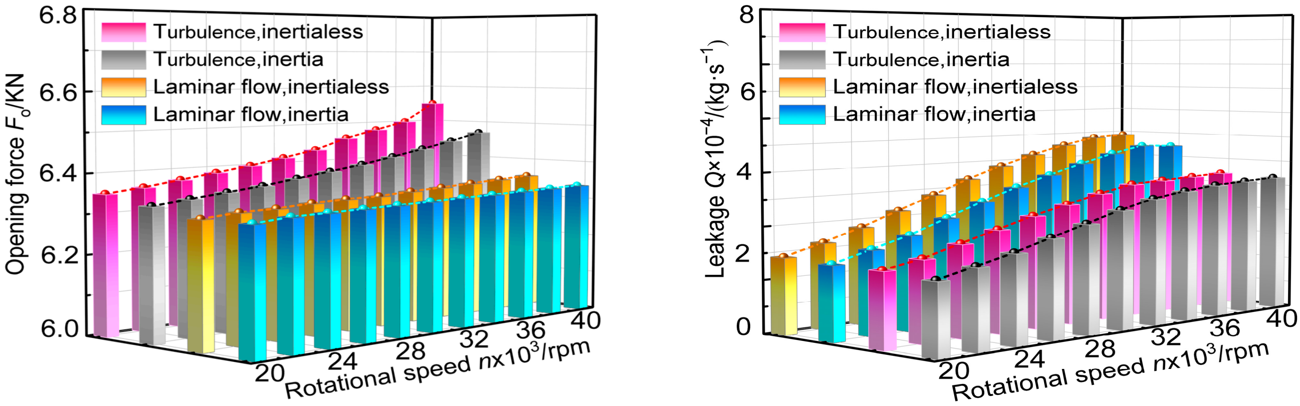

(**a**) Opening force (**b**) Leakage

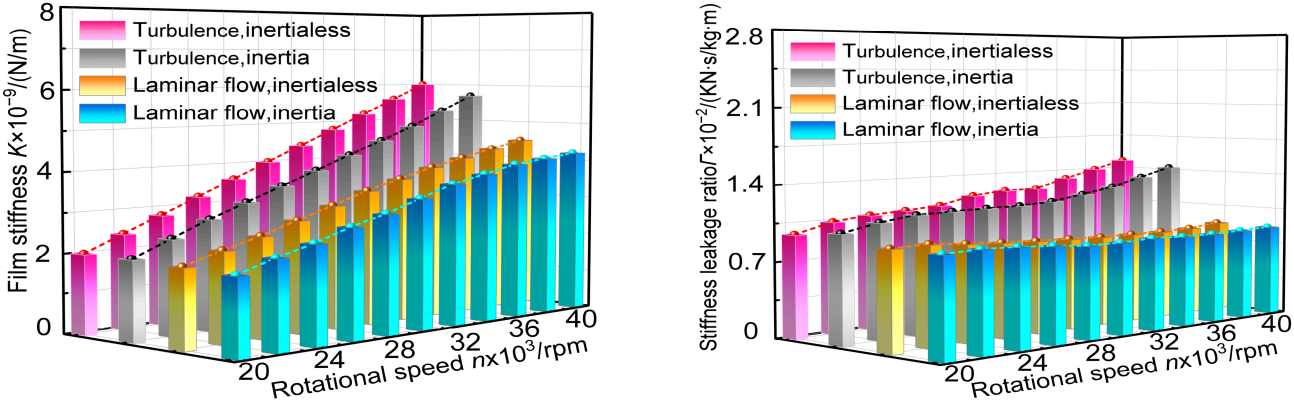

(**c**) Gas film stiffness (**d**) Stiffness leakage ratio

Figure 11. Effect of rotational speed on sealing performance.

5.3.2. Effect of Pressure on Sealing Performance

Figure 12 shows the variation rule of the dry gas seal performance parameters with pressure. Figure 12a shows that with an increase in medium pressure, the gas in the sealed area flowed from the high-pressure side to the low-pressure side, and that the dynamic pressure effect and opening force increased. The opening force is not affected by the flow state, it shows an obvious linear growth trend with the increase of pressure. The maximum relative error of the opening force was 1.51% when the inertia force effect was ignored; therefore, the influence of the inertia force effect on the opening force can be ignored when the high pressure difference was ignored. Figure 12b shows that when the turbulence effect was considered, the gas film outlet pressure decreased. Therefore, the leakage quantity under turbulent flow was lower than that under laminar flow. When p_o = 4 MPa, the maximum relative errors of the leakage quantity considering the inertia force effect were 1.18% and 1.65%. At this time, the turbulent effect under the high-pressure difference played a dominant role. Figure 12c shows that with an increase in the inlet pressure, the gas film stiffness first increased and subsequently decreased. The greater the pressure difference, the stronger the turbulence effect, and the higher the difference in gas film stiffness under different flow states. Figure 12d shows that the rigid leakage ratio declined as the pressure increased because the increase in the leakage was faster than the decrease in the stiffness. In addition, an increase in pressure led to a decrease in the gas film thickness and enhancement of the turbulence and inertia effects.

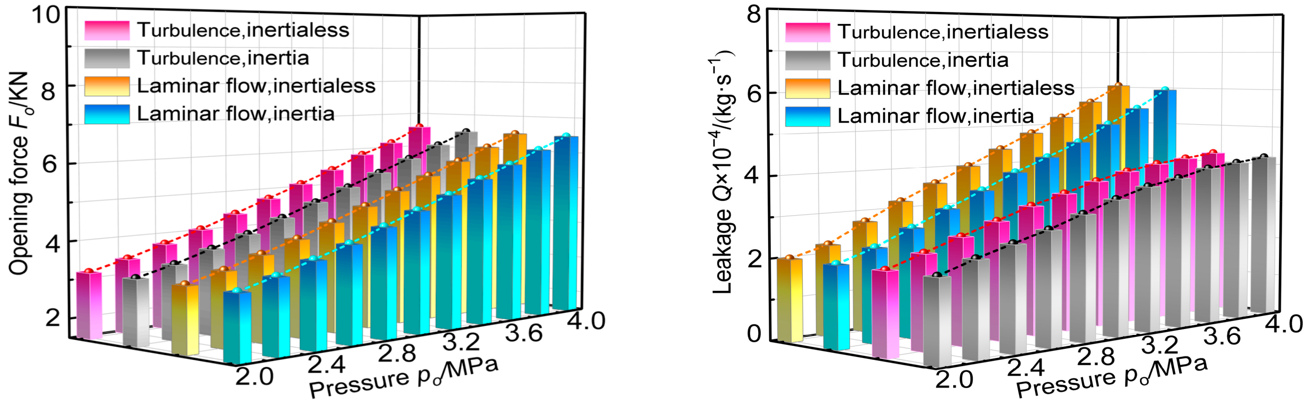

(**a**) Opening force (**b**) Leakage

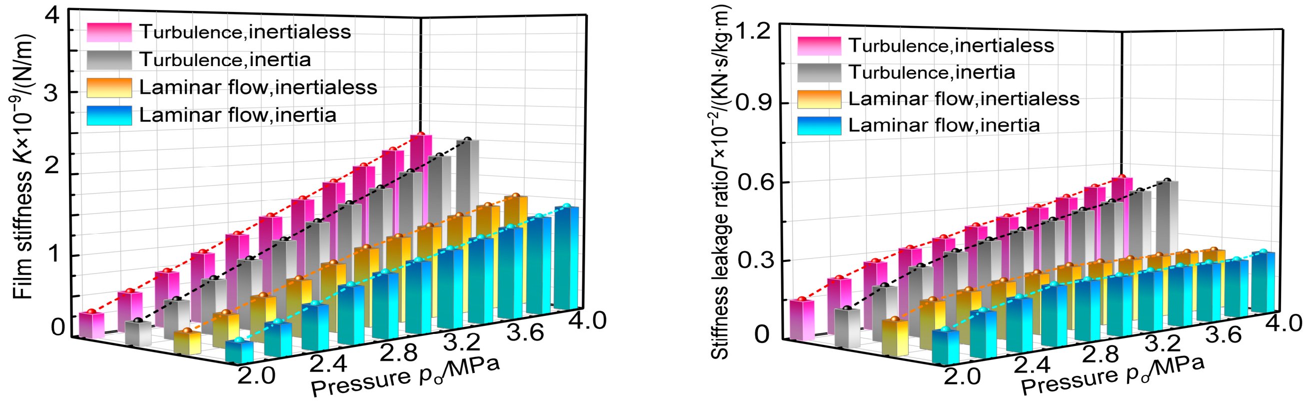

(**c**) Gas film stiffness (**d**) Stiffness leakage ratio

Figure 12. Effect of pressure on sealing performance.

5.3.3. Effect of Groove Depth on Sealing Performance

Figure 13 shows the variation rule of the dry gas seal performance parameters with respect to groove depth. As shown in Figure 13a, the opening force under turbulent flow with a groove depth of $h_g = 3$ μm was lower than that under laminar flow. When the groove depth increased to $h_g = 8$ μm, the turbulent effect became prominent and the opening force increased significantly with an increase in groove depth. Figure 13b shows that with the groove depth deepening, the leakage volume showed an overall increasing trend. The maximum relative errors were 0.5% and 2.9%. The leakage increased slowly with increasing groove depth, indicating that an increase in groove depth increased the height difference between the groove and non-T-groove region, weakening the pumping effect of the groove. When the groove depth was small, the leakage was minimally affected by inertia and can be ignored. With an increase in groove depth, the dynamic behavior of the gas film considering the inertia force effect became increasingly obvious. Figure 13c,d show the gas film stiffness and leakage, with respect to the groove depth in the laminar and turbulent flow states. When the groove depth was $h_g = 3$ μm, the atmospheric film stiffness and the rigid leakage ratio increased. When the gas film stiffness and rigid leakage were high, the influence of the turbulence and inertia effects was small, and the maximum relative error was less than 0.2%. However, with an increase in groove depth, the turbulence and inertia effects became prominent. Therefore, the inertia effect can be ignored when the groove depth is low, but the influence of the turbulence and inertia effects on dry gas seal performance should be considered as the groove depth increases.

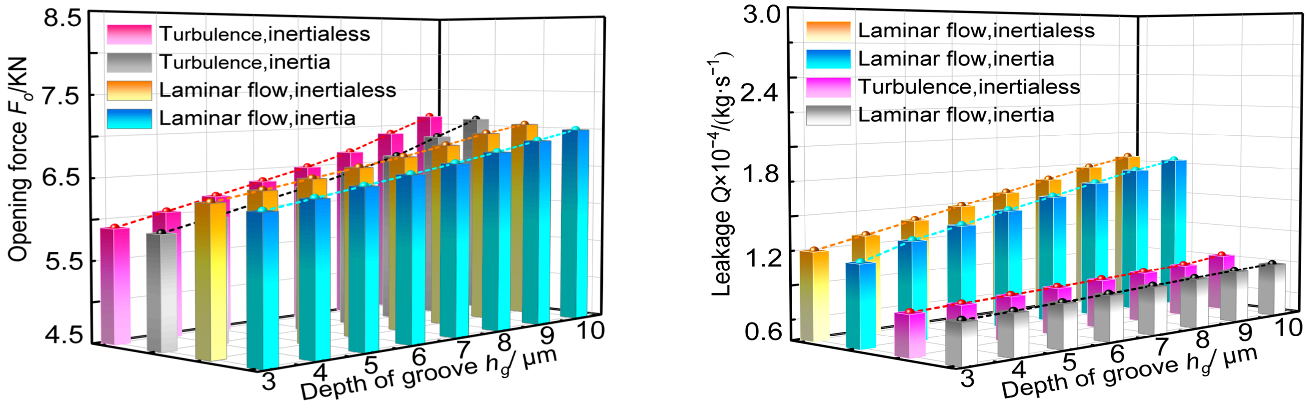

(**a**) Opening force (**b**) Leakage

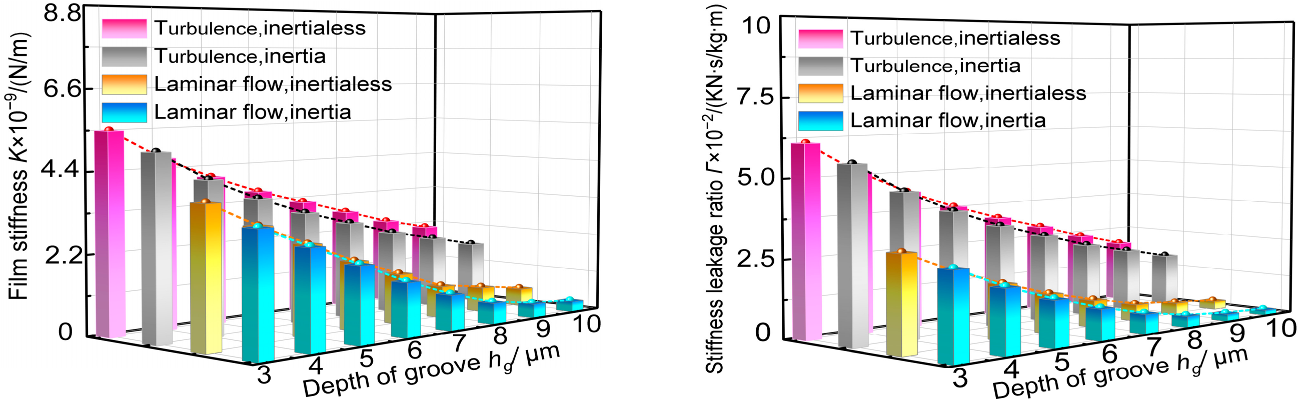

(**c**) Gas film stiffness (**d**) Stiffness leakage ratio

Figure 13. Effect of groove depth on sealing performance.

5.3.4. Effect of Gas Film Thickness on Sealing Performance

Figure 14 shows the variation rule of dry gas sealing performance parameters with respect to gas film thickness. The gas film thickness h_0 refers to the film thickness in the non-T-groove area. Figure 14 shows that when h_0 = 3 μm, the opening force and gas film stiffness were high. Figure 14a,c show that as the gas film thickness increased, the gas film flow area increased, and the gas film flow resistance decreased, resulting in a decrease in the opening force and stiffness of the gas film. Figure 14b, d show that a thick gas film easily led to gas flow instability, and thereby nonlinearly increased the leakage. Owing to the decrease and increase in gas film stiffness and leakage, the rigid leakage ratio decreased. Compared with laminar flow, the dynamic response of the gas film was considerably higher owing to the turbulent effect, and the fluid flow had higher kinetic energy and irregularity, resulting in higher opening force and stiffness of the gas film. In the non-T-groove region where the film thickness changed, the turbulent effect decreased the efficiency of conversion between the kinetic energy and static pressure of gas, increased energy loss, and reduced gas film stability. With an increase in film thickness, gas flow separation occurred in the T-groove, and the flow instability caused by the change in film thickness enhanced the possibility of occurrence of turbulence. In addition, the turbulence effect intensified the instability of flow inertia, which affected the sealing performance. The influence of the turbulence and inertia effects on the sealing performance can be further reduced by optimizing the structural parameters of the T-groove in the later stage.

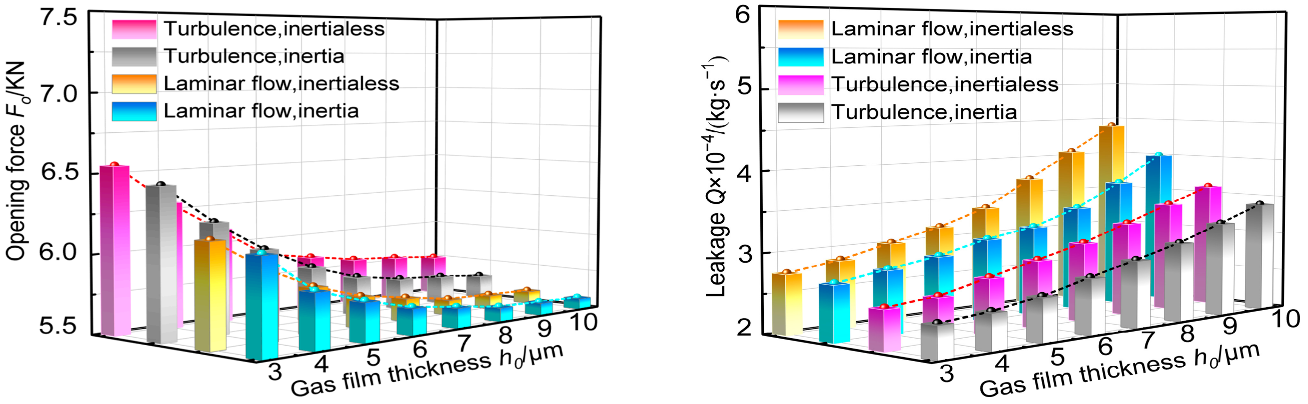

(**a**) Opening force (**b**) Leakage

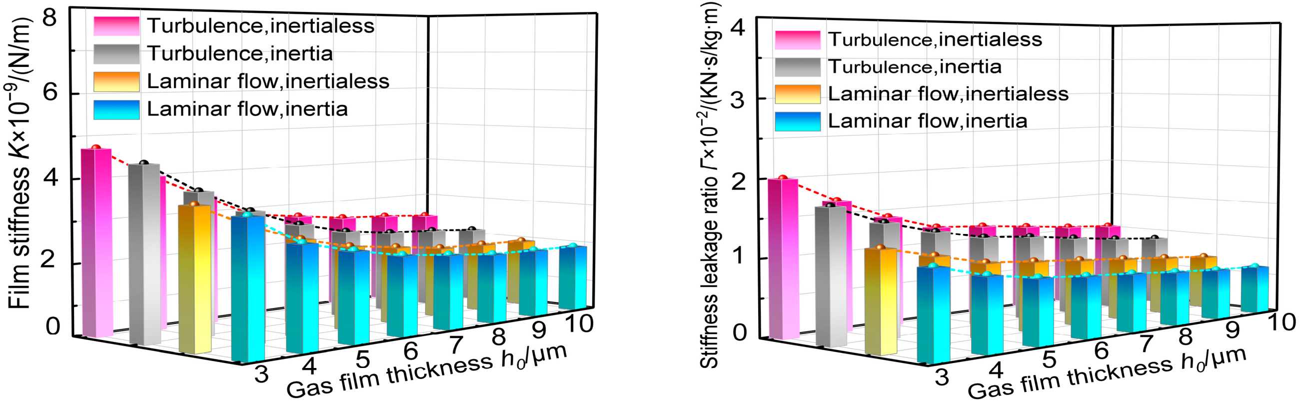

(**c**) Gas film stiffness (**d**) Stiffness leakage ratio

Figure 14. Effect of gas film thickness on sealing performance.

6. Conclusions

In this study, the Reynolds equation that considers the interaction between centrifugal inertia force and turbulence effects was solved to obtain the film pressure distribution for the modified gas lubrication and the variation patterns of different flow state of sealing performance.

(1) When rotational speed was 40,000 rpm, the opening force increased by 0.7% and 3.1% under the laminar and turbulent flow states, respectively. With an increase in n, the turbulent effect on gas film became prominent. Considering the turbulent effect, the radial mean speed decreased; therefore, the leakage under turbulent flow was less than that under laminar flow.

(2) When the pressure was 4 MPa, the maximum relative errors of leakage considering the inertia force effect were 1.18% and 1.65%. At this time, the turbulent effect under the high-pressure difference plays a dominant role. The greater the pressure difference, the stronger the turbulence effect and the greater the difference in the stiffness of the gas film under different flow states. Because the increase in the leakage is faster than the decrease in the stiffness, the rigid leakage ratio tends to decrease.

(3) When the groove depth was 3 μm, the influence of the inertia effect on the sealing performance was negligible. The opening force in the turbulent flow state was slightly lower than that under the turbulent flow mode, but the atmospheric film stiffness and rigid leakage ratio in the former state were higher than in the latter state. When the groove depth was increased to 8 μm, the height difference between the trough and non-T-groove region increased, and the turbulent effect became prominent.

(4) When the gas film thickness was 3 µm, the opening force and gas film stiffness were high. Owing to the strong dynamic pressure effect in the small film thickness groove, the turbulence effect changed considerably. The turbulence effect intensified the instability of flow inertia, which zoned the sealing performance.

Author Contributions: Conceptualization, X.D.; methodology, L.Z.; formal analysis, S.W.; investigation, S.Z.; resources, S.W.; data curation, S.W.; writing—original draft preparation, L.Z.; visualization, S.W.; supervision, S.Z.; project administration, L.Z. All authors have read and agreed to the published version of the manuscript.

Funding: The research was supported by the National Natural Science Foundation of China (no. 51565029).

Data Availability Statement: Data are contained within the article.

Acknowledgments: The authors are grateful to the reviews for their careful and detailed comments.

Conflicts of Interest: The authors declare no conflicts of interest.

References

1. Wu, F.; Jiang, J.; Peng, X.; Teng, L.; Meng, L.; Li, J. Influence of natural gas composition and operating conditions on the steady-state performance of dry gas seals for pipeline compressors. *J. Lubr.* **2024**, *12*, 217. [CrossRef]
2. Yin, C.; Li, Y.; Wang, Y.; Dong, Y. Physics-guided degradation trajectory modeling for remaining useful life prediction of rolling bearings. *J. Mech. Syst. Signal Process.* **2025**, *224*, 112192. [CrossRef]
3. Du, Q.; Gao, K.; Zhang, D.; Xie, Y. Effects of grooved ring rotation and working fluid on the performance of dry gas seal. *Int. J. Heat Mass Transf.* **2018**, *126*, 1323–1332. [CrossRef]
4. Hu, L.; Wang, Z.; Wang, J.; Wang, Y. Derivative analysis and evaluation of roll-slip fretting wear mechanism of ultra-thin-walled bearings under high service. *J. Wear* **2024**, *562*, 205630. [CrossRef]
5. Hu, L.; Li, B.; Wang, Z.; Wang, Y. Analysis and evaluation of multi-state wear mechanism of elastic-flexible thin-walled bearings. *J. Tribol. Int.* **2025**, *202*, 110293. [CrossRef]
6. Tahan, M.R. Recent advances in hydrogen compressors for use in large-scale renewable energy integration. *Int. J. Hydrogen Energy* **2022**, *47*, 35275–35292. [CrossRef]
7. Koga, T.; Fujita, T. The hydrostatic noncontact seal including fluid inertia effect. *J. ASLE Trans.* **1986**, *29*, 35–42. [CrossRef]
8. Zhang, X.; Meng, X.; Liang, Y.; Peng, X. Steady performance on high-speed spiral-grooved mechanical seals based on turbulent model. *J. Tribol.* **2020**, *40*, 260–270.
9. Shahin, I.; Gadala, M.; Alqaradawi, M.; Badr, O. Three dimensional computational study for spiral dry gas seal with constant groove depth and different tapered grooves. *J. Proc. Eng.* **2013**, *68*, 205–212. [CrossRef]
10. Hahn, M.; Park, Y.; Kang, M.; Jun, S.; Jang, G. Effects of laminar, turbulent, and slip conditions in a fluid film on a dry gas seal. *J. Mach.* **2022**, *10*, 954. [CrossRef]
11. Park, Y.; Hahn, M.; Jang, G. Effect of laminar, turbulent and slip conditions on the dynamic coefficients of a dry gas seal. *J. Lubr.* **2023**, *11*, 98. [CrossRef]
12. Yan, R.; Chen, H.; Zhang, W.; Hong, X.; Bao, X. Calculation and verification of flow field in supercritical carbon dioxide dry gas seal based on turbulent adiabatic flow model. *J. Tribol. Int.* **2022**, *165*, 107275. [CrossRef]
13. Ding, X.; Jiang, H.; Xu, J.; Yan, R.; Ding, J. Research progress of turbulence effect on dry gas sealing peformance. *J. Lubr. Eng.* **2023**, *48*, 188–195.
14. Wang, Y.; Hao, Z.; Wu, J. Investigation on the dynamic characteristics for high-speed mechanical seal considering turbulent cavitating flow and inertia effect. *J. Ind. Lubr. Tribol.* **2024**, *76*, 864–872. [CrossRef]
15. Xu, H.; Song, P.; Mao, W.; Deng, Q. The performance of spiral groove dry gas seal under choked flow condition considering the real gas effect. *Proc. Ins. Mec. Eng. Part J Eng. Tribol.* **2020**, *234*, 554–566. [CrossRef]
16. Yuan, T.; Yang, R.; Li, Z.; Yang, Q.; Song, L. Thermal characteristics and cooling effect for SCO_2 dry gas seal with multiple dynamic groove types. *J. Appl. Therm. Eng.* **2024**, *236*, 121896. [CrossRef]
17. Mo, L.; Ding, X.; Yan, R.; Wang, S. Steady-state performance analysis of dry gas seal with imitation tree groove. *J. Lubr. Eng.* **2022**, *47*, 68–74.
18. Ma, Y.; Peng, X.; Bai, S.; Meng, X.; Gu, T. Analysis of hydrodynamic characteristics of bi-direction fir tree groove gas face seal. *J. Fluid Mach.* **2012**, *40*, 13–16.

19. Hu, Q.; Zhu, M.; Wang, Y.; Tang, X.; Xu, W.; Zheng, X. Performance analysis of firtree-groove dry gas seal with radial orderly micro-structure. *J. Sichuan Univ. (Eng. Sci. Ed.) China* **2020**, *52*, 153–160.
20. Wang, Y.; Hu, Q.; Sun, J.; Wang, D.; Zhen, X. Numerical analysis of T-groove dry gas seal with orientation texture at the groove bottom. *J. Adv. Mech. Eng.* **2019**, *11*, 1687814018821775.
21. Zhang, C.; Jiang, J.; Zhao, W.; Jin, J.; Peng, X. A Comprehensive Multi-Objective, Multi-Parameter and Multi-Condition Optimization of a Spiral Groove in Dry Gas Seals. *J. Braz. Soc. Mech. Sci. Eng.* **2022**, *44*, 206. [CrossRef]
22. Johansson, P.; Marklund, P.; Björling, M.; Shi, Y. Effect of roughness on the running-in behavior and tribofilm formation of carbon fiber reinforced PTFE composite in trace moisture environment. *J. Wear* **2022**, *500*, 204367. [CrossRef]
23. Kim, T.W.; Callas, C.; Saltzer, S.D.; Kovscek, A.R. Assessment of oil and gas fields in California as potential CO_2 storage sites. *Int. J. Greenh. Gas Control* **2022**, *114*, 103579. [CrossRef]
24. He, T.; Zhang, Q.; Yan, Y.; Dong, J.; Zhou, P. Numerical simulation of a new designed mechanical seals with spiral groove structures. *J. Lubr.* **2023**, *11*, 70. [CrossRef]
25. Chávez, A.; De Santiago, O. Experimental Measurements of the Thermo Elastic Behavior of a Dry Gas Seal Operating with Logarithmic Spiral Grooves of 11° and 15°. *Proc. Inst. Mech. Eng. Part J J. Eng. Tribol.* **2021**, *235*, 1807–1819. [CrossRef]
26. Fairuz, Z.M.; Jahn, I.; Abdul-Rahman, R. The effect of convection area on the deformation of dry gas seal operating with supercritical CO_2. *J. Tribol. Int.* **2019**, *137*, 349–365. [CrossRef]
27. Li, X.; Meng, X.; Zhao, W.; Peng, X. Numerical investigation on a hybrid porous-spiral groove mechanical face seal. *J. Tribol. Int.* **2024**, *198*, 109943. [CrossRef]
28. Teng, L.; Jiang, J.; Peng, X.; Li, J. Influence of surface grooving methods on steady and dynamic performance of spiral groove gas face seals. *J. Alex. Eng. J.* **2023**, *64*, 55–80. [CrossRef]
29. Shen, W.; Peng, X.; Jiang, J.; Li, J. Analysis on real effect of supercritical carbon dioxide dry gas seal at high speed. *CIESC J.* **2019**, *70*, 2645–2659.
30. Constantinescu, V.N.; Galetuse, S. On the possibilities of improving the accuracy of the evaluation of inertia Forces in laminar and turbulent films. *J. Lubr. Technol.* **1974**, *96*, 69–77. [CrossRef]
31. Xu, H.; Song, P.; Mao, W.; Deng, Q.; Sun, X. Analysis on inertia effect of carbon dioxide dry gas seal at high speed and pressure under laminar condition. *CIESC J.* **2018**, *69*, 4311–4323.
32. Yan, R.; Chai, B.; Ma, L.; Chen, H.; Ding, X. Dynamic coefficient investigation for supercritical carbon dioxide dry gas seal based on complete variable perturbation model. *J. Lubr.* **2024**, *12*, 298. [CrossRef]